Calhoun
Institutional Archive of the Naval Postgraduate School

Calhoun: The NPS Institutional Archive

DSpace Repository

Faculty and Researchers | Faculty and Researchers' Publications

2017-02

Variability of upper ocean thermohaline structure during a MJO event from DYNAMO aircraft observations

Alappattu, Denny P.; Wang, Qing; Kalogiros, John; Guy, Nick; Jorgensen, David P.

Alappattu, Denny P., et al. "Variability of upper ocean thermohaline structure during a MJO event from DYNAMO aircraft observations." Journal of Geophysical Research: Oceans 122.2 (2017): 1122-1140.
http://hdl.handle.net/10945/55113

This publication is a work of the U.S. Government as defined in Title 17, United States Code, Section 101. Copyright protection is not available for this work in the United States.

Downloaded from NPS Archive: Calhoun

http://www.nps.edu/library

Calhoun is the Naval Postgraduate School's public access digital repository for research materials and institutional publications created by the NPS community. Calhoun is named for Professor of Mathematics Guy K. Calhoun, NPS's first appointed -- and published -- scholarly author.

Dudley Knox Library / Naval Postgraduate School
411 Dyer Road / 1 University Circle
Monterey, California USA 93943

AGU PUBLICATIONS

JGR

Journal of Geophysical Research: Oceans

RESEARCH ARTICLE

10.1002/2016JC012137

Key Points:
- In situ observations are made from the tropical Indian Ocean using airborne expendable probes deployed from P-3 Orion aircraft
- Response of mixed layer, isothermal layer, and thermocline is analyzed with respect to the different phases of MJO in the Indian Ocean
- In the active phase of MJO, the mixed layer depth showed a bimodal distribution

Correspondence to:
D. P. Alappattu,
dpalappa@nps.edu

Citation:
Alappattu, D. P., Q. Wang, J. Kalogiros, N. Guy, and D. P. Jorgensen (2017), Variability of upper ocean thermohaline structure during a MJO event from DYNAMO aircraft observations, *J. Geophys. Res. Oceans*, *122*, 1122–1140, doi:10.1002/2016JC012137.

Received 8 JUL 2016
Accepted 5 JAN 2017
Accepted article online 10 JAN 2017
Published online 13 FEB 2017

© 2017. American Geophysical Union. All Rights Reserved.

Variability of upper ocean thermohaline structure during a MJO event from DYNAMO aircraft observations

Denny P. Alappattu[1,2], Qing Wang[1], John Kalogiros[3], Nick Guy[4], and David P. Jorgensen[5]

[1]Meteorology Department, Naval Postgraduate School, Monterey, California, USA, [2]Moss Landing Marine Laboratories, San Jose State University, Monterey, California, USA, [3]Institute of Environmental Research and Sustainable Development, National Observatory of Athens, Athens, Greece, [4]Department of Atmospheric Science, University of Wyoming, Laramie, Wyoming, USA, [5]NOAA/National Severe Storms Laboratory, Norman, Oklahoma, USA

Abstract This paper reports upper ocean thermohaline structure and variability observed during the life cycle of an intense Madden Julian Oscillation (MJO) event occurred in the southern tropical Indian Ocean (14°S–Eq, 70°E–81°E). Water column measurements for this study were collected using airborne expendable probes deployed from NOAA's WP-3D Orion aircraft operated as a part of Dynamics of MJO field experiment conducted during November–December 2011. Purpose of the study is twofold; (1) to provide a statistical analysis of the upper ocean properties observed during different phases of MJO and, (2) to investigate how the upper ocean thermohaline structure evolved in the study region in response to the MJO induced perturbation. During the active phase of MJO, mixed layer depth (MLD) had a characteristic bimodal distribution. Primary and secondary modes were at ∼34 m and ∼65 m, respectively. Spatial heterogeneity of the upper ocean response to the MJO forcing was the plausible reason for bimodal distribution. Thermocline and isothermal layer depth deepened, respectively, by 13 and 19 m from the suppressed through the restoring phase of MJO. Thicker (>30 m) barrier layers were found to occur more frequently in the active phase of MJO, associated with convective rainfalls. Additionally, the water mass analysis indicated that, in the active phase of this MJO event the subsurface was dominated by Indonesian throughflow, nonetheless intrusion of Arabian Sea high saline water was also noted near the equator.

1. Introduction

The Madden Julian Oscillation (MJO) is the dominant intraseasonal variability in the tropics, most active in the Indian and Western Pacific Oceans, characterized by large-scale atmospheric convection anomaly propagating eastward with a time period of 30–60 days [*Madden and Julian*, 1972; *Zhang*, 2005]. MJO influences all the major tropical weather phenomena such as the Asian summer monsoon, El Niño-southern oscillation (ENSO), and Indian Ocean dipole [*Pai et al*., 2011; *Hendon et al*., 2007; *Han et al*., 2006; *Saji et al*., 1999] as well as extra tropical weather and climate [e.g., *Thompson and Roundy*, 2013; *Flatau and Kim*, 2013; *Cassou*, 2008].

Considerable progress has been made in the MJO research during the past few decades through the concerted efforts such as TOGA-COARE field experiment conducted in the western Pacific warm pool [*Webster and Lukas*, 1992]. However, numerical models are not very successful in forecasting the MJO or reproducing the past MJO signals [*Jiang et al*., 2015; *Sperber and Kim*, 2012; *Lin et al*., 2006]. Recent model fidelity studies emphasized the need of understanding the air-sea interaction taking place on the time scale of MJO [*Jiang et al*., 2015; *Woolnough et al*., 2007]. Air-sea interaction takes place, respectively, at the top and bottom boundaries of ocean mixed layer (OML) and marine atmospheric boundary layer (MABL) through the exchange of heat, mass, and momentum. Large-scale convection and anomalous zonal wind governs the surface flux in the active phase of MJO. Convective clouds prevent the insolation from reaching the ocean surface, producing strong sea surface temperature (SST) cooling [*Shinoda et al*., 1998; *Hendon and Glick*, 1997]. Enhanced wind stress affects the upper ocean dynamics, which include the modification of the SST through surface latent and sensible heat fluxes [e.g., *Duvel et al*., 2004]. Furthermore, strong winds boost the upwelling and entrainment, mechanical stirring and horizontal advection [*Drushka et al*., 2012; *Saji et al*., 2006; *Waliser et al*., 2003; *Cronin and McPhaden*, 1997]. Additionally, excess precipitation over evaporation produces positive net freshwater flux in to the ocean surface. These different surface processes modulate

the upper ocean temperature and salinity stratification that determines the mixed layer and the thermocline variability. Presence of a barrier layer [*Lukas and Lindström*, 1991] also may play a role in the response of the mixed layer temperature to atmospheric forcing [*Shinoda and Hendon*, 1998; *Schiller and Godfrey*, 2003]. In short, during a MJO event, the flux perturbations affect ocean thermohaline structure and this in turn affects the mixed layer temperature and the SST that can influence the MJO characteristics. The knowledge on the variability of the thermohaline structure of the ocean would be then a useful factor for predicting the MJO features on seasonal scale.

As mentioned above, atmospheric variability associated with the MJO exerts great impact on the upper ocean thermohaline structure. Using the ship borne observations in Western Pacific Ocean, *Lukas and Lindstrom* [1991] showed that the SST cooled by more than 1° and the mixed layer deepened from 22 to 44 m during an intense MJO event. While the anomalous latent heat flux accounted for much of the surface cooling mixed layer deepening was attributed to the wind induced mechanical stirring. TOGA-COARE measurements were highly successful in understanding the Western Pacific warm pool temperature and salinity behavior during the propagation of MJOs [e.g., *Hendon and Glick*, 1997; *Shinoda and Hendon*, 1998].

Many of the previous Indian Ocean MJO studies were based on satellite observations and/or model output. A few in situ studies are also have reported from this region, using the single point observations from moorings or utilizing the limited Argo float data [*Argo*, 2000]. Majority of these earlier studies were devoted to divulge the physical processes responsible for intense intraseasonal SST cooling events in the Indian Ocean occurring during boreal winters. *Harrison and Vecchi* [2001] and *Duvel et al*. [2004] showed that the SST cooling during the individual MJO events could be as high as 3°C and most events cooled the SST by about 1.5°C. *Harrison and Vecchi* [2001] argued that the air-sea fluxes alone cannot account for such large amount of cooling and oceanic subsurface processes also should be involved. However, by examining two SST cooling events during 1999, *Duvel et al*. [2004] suggested that the anomalous SST perturbation during MJO was driven by air-sea heat fluxes and not by advection or subsurface exchange. Later on, *Saji et al*. [2006] and *Vinayachandran and Saji* [2008] identified air-sea flux as the dominant cooling mechanism when the thermocline was deep and mixed layer was thick. Whereas, the entrainment dominated when the thermocline was shallow. In the southern tropical Indian Ocean, shallow mean thermocline often observed in the latitude range from ∼2.5°S to ∼14°S that extends eastward as a ridge to about 90°E [*Hermes and Reason*, 2008]. This is known as the Seychelles Chagos thermocline ridge (SCTR). Thermocline ridge is maintained by Ekman pumping associated with a northward weakening of the southeasterly trade winds [*Foltz et al*., 2010; *Vialard et al*., 2009; *Saji et al*., 2006].

All these studies provided enough evidence for large perturbations that takes place in the tropical Indian Ocean on MJO time scale. However, the intraseasonal variability of mixed layer, isothermal layer, and/or the barrier layer occurring in the Indian Ocean remained largely overlooked. Recent increase in water column observations using Argo floats shed light on the spatial pattern of variability of thermohaline structure in the Indo-Pacific basin. For example, *Matthews et al*. [2010] used Argo data to characterize MJO-related anomalies of temperature and salinity throughout the water column. This study revealed that patterns of anomalous mixed layer temperature produced by the anomalies in heat flux during MJO event. *Drushka et al*. [2012] studied the response of the ocean mixed layer to the MJO in the Indo-Pacific region using the Argo data set. They showed that the MJOs could induce systematic variations in mixed layer depth greater than 15 m and temperature amplitude changes up to 0.6°C in the Indian Ocean. Examining the Argo and mooring data, *Drushka et al*. [2014] reported large swings in mixed layer depth and isothermal layer depth occurring in the eastern equatorial Indian Ocean during MJO events. More in situ studies are, however, still requested from tropical Indian Ocean to understand the coupled ocean-atmosphere processes over the MJO cycle [*DeMott et al*., 2015]. In this context, this study provides a statistical analysis on the variability of upper ocean properties observed during different phases of an intense MJO in the tropical Indian Ocean and also examines the upper ocean thermohaline structure response to the MJO forcing.

This paper reports the variability of the parameters such as mixed layer depth (MLD), isothermal depth (ILD), barrier layer thickness (BLT), thermocline, and SST observed in the different phases of an intense MJO event. For this analysis, we used in situ observations made from a large region in the Indian Ocean (14°S to equator and 70°E to 81°E; Figure 1) measured by the expendable probes deployed from aircraft (NOAA WP-3D Orion: P-3). The observations spanned through the entire life cycle of a MJO. The study also attempts to explain the observed variability by examining MJO induced the upper ocean evolution observed at two

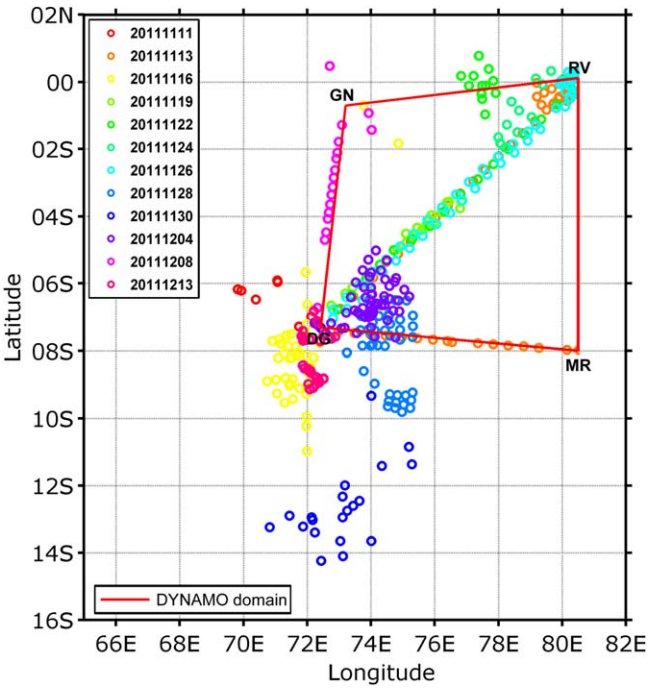

Figure 1. DYNAMO domain with locations of AXBT/AXCTD drops color coded for each flight day. Positions of research vessels (RV: R/V Revelle and MR: R/V Mirai) and the island stations (DG: Diego Garcia and GN: Gan) are also shown.

moored buoys. This demonstrates, how disparate is the upper ocean response to the MJO forcing at different locations separated even by small distance (compared with planetary spatial scale of MJO). This report is unique in the sense that, the results represents the MJO induced upper ocean perturbation from a large spatial region from the data sparse and climatically important southern tropical Indian Ocean.

2. Data and Methods

2.1. LASP/DYNAMO and NOAA P-3 Measurements

Considering the importance of the Indian Ocean for the initiation of MJO, Dynamics of MJO (DYNAMO) field campaign was conducted in the tropical Indian Ocean in association with the cooperative Indian Ocean experiment on intraseasonal variability (CINDY) during 1 October 2011 to 31 March 2012 [*Yoneyama et al.*, 2013]. Littoral Air Sea Processes (LASP) program sponsored the measurements of air-sea processes based on ships and research aircrafts. Domain of DYNAMO field experiment was roughly in the latitude range from 10°S and equator within the longitudes ranging from 70°E to 81°E (Figure 1). Time series mode of observations were conducted from the research vessels R/V Revelle (RV) and R/V Mirai (MR) and the island stations set up at Diego Garcia (DG) and Gan (GN) [*Johnson et al.*, 2013; *Moum et al.*, 2014]. Although fixed point measurements are very useful to study the temporal variability of the phenomena, the results often may not be representative of the domain wide variability, which is especially pertinent for planetary scale atmospheric and/or oceanic processes such as MJO. Keeping this in mind, during DYNAMO, P-3 observations were made specifically between ship and island stations and mostly in the study domain to complement the fixed point observations [*Chen et al.*, 2016]. P-3 observations spanned in the latitudes between 14°S and equator within 70°E–81°E longitude region. P-3 made several sorties (see Figure 1, for dates of P-3 operation) in the DYNAMO special observation period (DYNAMO SOP; November–December 2011) and gathered data from flight level mean and turbulence measurements, radar remote sensing of clouds as well as by profiling the atmosphere and ocean, respectively using dropsondes and Airborne Expendable Conductivity-Temperature-Depth (AXCTD) and Airborne Expendable Bathythermographs (AXBT). Water column measurements by the AXCTDs and AXBTs are the primary data set for this study.

2.2. AXCTD/AXBT Data and Layer Definition

AXCTD/AXBT probes measure the ocean temperature and salinity similarly to their shipborne counterparts, expendable conductivity-temperature-depths (XCTDs), and expendable bathythermographs (XBTs) [e.g., *Yabuki et al.*, 2006; *Levitus et al.*, 2009; *Stephenson et al.*, 2012]. While AXBT measures the water temperature and depth, the AXCTD additionally provides the water column salinity measurements too. Airborne measurements provide several advantages over those made by XCTDs/XBTs. For example, with the high mobility of an aircraft, AXCTD/AXBT can sample a relatively large area within a short time period, providing spatial variability of the upper ocean down to 1000 m depth with vertical resolutions of less than 1 m. Procedure of deployment and data collection using AXCTD/AXBT is briefly described here. AXCTD/AXBT probes launched from the aircraft are slowed down with a small parachute to reduce the impact speed at the ocean surface. Upon impact, a small buoy inflates to host the radio transmitter. Seawater activates the battery and turns on the transmitter. After establishing communication with the aircraft-based radio frequency

Table 1. Summary of AXCTD/AXBT Data Successfully Retrieved During DYNAMO

Date	November 11	November 13	November 16	November 19	November 22	November 24	November 26	November 28	November 30	December 4	December 8	December 13		Success
Flight	RF01	RF02	RF03	RF04	RF05	RF06	RF07	RF08	RF09	RF10	RF11	RF12	Total	Rate
AXBT	5	48	24	9	20	9	39	28	18	51	17	28	296	92.2%
AXCTD	2	4	16	17	11	2	22	16	4	4	0	11	109	95.6%

(RF) receiver, the probe is released from its canister and descends through the water column. The probe sends measurements to its surface unit inside the buoy, connected by a thin copper wire, and the surface unit transmits data to the aircraft-based RF receiver. Data Acquisition System processes the signal in real time and archives the ASCII data. Strict quality control was applied to the AXCTD/AXBT data before the analysis. Details of data quality issues and specific steps taken to correct the erroneous data can be found in *Alappattu and Wang* [2015]. Quality and consistency of AXCTD data were confirmed by comparisons with the independent CTD measurements [*Alappattu and Wang*, 2015]. These procedures yielded a total of 296 AXBT profiles and 109 AXCTD profiles. Figure 1 shows the AXCTD/AXBT probe launch location with respect to DYNAMO domain. Table 1 summarizes number of the AXCTD/AXBT profiles taken on each day of flight. Success rate indicates the efficiency of the data retrieval method. In order to reduce the latitudinal variability, only profiles taken north of 10°S were considered for this analysis. In addition to the AXCTD/AXBT data, we have also used NOAA interpolated outgoing longwave radiation (OLR) data set [*Liebmann and Smith*, 1996; http://www.esrl.noaa.gov/psd/] and research moored array for African-Asian-Australian monsoon analysis and prediction (RAMA) buoy data available from http://www.pmel.noaa.gov/.

From the temperature and density profiles, ILD and MLD were calculated using the threshold method as defined by *Sprintall and Tomczak* [1992]. The data were linearly interpolated to a vertical resolution of 0.5 m. The ILD was defined as the depth where the temperature was lower by 0.5°C from that at 10 m depth. Using AXCTD derived density profile, MLD was calculated in terms of a depth where the density was equal to the density at 10 m plus the increment in density equivalent to 0.5°C. Density increment was determined by the coefficient of thermal expansion. Temperature and salinity at 10 m was used for the computation of coefficient of thermal expansion.

In regions where upper ocean salinity stratification is weak, temperature stratification determines the base of the mixed layer, and the MLD is equal to the ILD. If salinity dominates the upper ocean stratification, MLD can be shallower than ILD. The layer separating the bottom of MLD and ILD is defined as the barrier layer (BL) and the thickness is referred to as the barrier layer thickness (BLT) [*Cronin and McPhaden*, 2002; *Girishkumar et al*., 2011; *Qiu et al*., 2012]. *Cronin and McPhaden* [2002] describe the different mechanisms that produce barrier layers (BLs) including the effect of rainfall. Even though convective rain falls produce BLs of considerable thickness, increased wind induced upper ocean mixing during the active phase of MJO often erodes these BLs [*Zhang and McPhaden*, 2000]. But in the presence of zonal and meridional salinity gradients, the equatorial ocean response to westerly wind bursts (WWB) can include the formation of thick, long lived BLs [*You*, 1995; *Cronin and McPhaden*, 2002].

3. Evolution of MJO and General Meteorological Conditions

This section briefly describes the evolution of the MJO event, also known as MJO2 or November MJO [*Yoneyama et al*., 2013] occurred during the DYNAMO SOP. General meteorological conditions observed during the MJO event are also described. Overall atmospheric and oceanic conditions observed during the entire DYNAMO experiment can be referred to *Yoneyama et al*. [2013] and *Gottschalck et al*. [2013]. Hovmöller diagram of OLR anomalies from 10 November to 15 December 2011 in the latitude range from 20°S to 20°N averaged over 72°E to 81°E longitude is shown in Figure 2. Anomalies were calculated from the long term mean taken over a period from 1981 to 2010. Strong negative OLR anomalies (with magnitudes greater than 80 W m^{-2}) associated with active MJO convection occurred from 22 to 30 November 2011. Negative OLR anomaly was large and widespread at north of equator in comparison to corresponding southern latitudes. Prior to the onset of MJO (or during the suppressed phase of MJO), convection within ITCZ was prevalent in the southern DYNAMO domain. In the figure, this can be distinguished by the

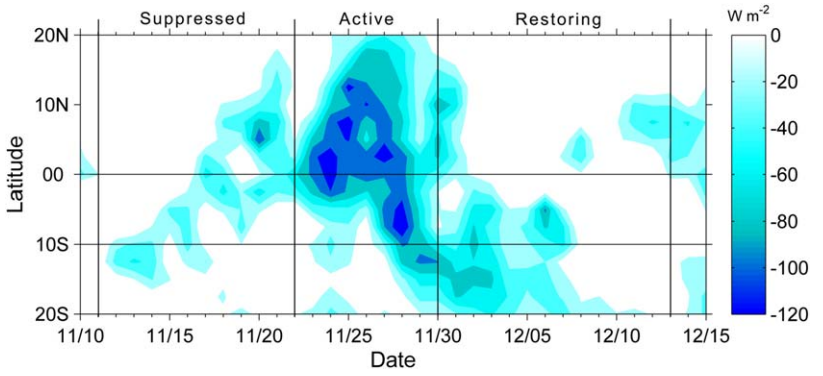

Figure 2. Hovmöller diagram of OLR anomalies from 10 November to 15 December 2011 in the latitude range from 20°S to 20°N averaged over the 72°E to 81°E.

negative OLR anomalies seen from 12 to 20 November. ITCZ migrated from southern latitudes (~15°S) and crossed the equator a few days before the onset of active phase of MJO in the Indian Ocean. Convection in northern latitudes ceased soon after the active phase of MJO. Meanwhile, south of equator experienced sustained convection even after the active phase of the MJO. In this paper, MJO suppressed phase refers to the aircraft observation period from 11 November to 21 November 2011 and active period of MJO was from 22 November to 30 November 2011. MJO activity in the Indian Ocean became inactive by the beginning of the December. This post-MJO suppressed period (aircraft observation period from 1 December to 13 December 2011) is referred to as the restoring phase [*Yoneyama et al.*, 2013]. MJO phases are demarcated in Figure 2 using vertical lines.

Figures 3a–3d show the variability of sea surface temperature, air temperature, wind speed, and relative humidity observed by RAMA buoys located at 8°S, 4°S, 1.5°S, and equator along the 80.5°E. These plots are indented to provide a general view of the latitudinal extent and variability of the MJO signal as reflected in meteorological variables. At 1.5°S and equator highest SST observed was in suppressed phase and lowest toward the end of active phase. MJO signal was not very significant in the SST at 4°S. Interestingly, at 8°S seasonal forcing (due to the transition from spring to summer in the southern hemisphere) of SST was stronger than the MJO associated variability. Similar to SST, differences were there in the response of air temperature, wind speed as well as relative humidity to the MJO signal at different latitudes. However, average air temperature was the lowest and wind speed as well as relative humidity was the highest in the active phase of MJO.

4. Results

4.1. Upper Ocean Profiles and Variability of MLD, ILD, BLT, D20, and SST

Figures 4a–4c illustrate three typical types of upper ocean profiles observed during DYNAMO. Profiles were taken during the active MJO phase but on two different days from different locations. Temperature, salinity, and potential density profiles in Figure 4a were taken on 26 November during 0509 Z at 3.79°S and 76.22°E. Here the separation between MLD and ILD was only 2 m and hence BL was very thin. Mean ILD temperature was approximately 29.16°C. Profiles shown in Figure 4b were taken on 28 November during 0512 Z at 7.20°S and 74.60°E. From the density and temperature profiles, the MLD and ILD were estimated as 31 and 67 m, respectively. Considerable difference between ILD and MLD resulted in a thick (36 m) BL in this case. ILD temperature remained nearly uniform around 28.90°C. In the former case the upper ocean salinity stratification was weak. Therefore, the MLD as well as ILD was determined primarily by the temperature stratification and hence BL was very thin or practically nonexistent. But the upper ocean salinity stratification was strong in the latter case. Therefore, the salinity stratification was responsible for shallow MLD, meanwhile the well mixed temperature layer produced deeper ILD. Unlike the 26 November profile the measurement on 28 November was taken during precipitation. The haline stratification and hence the shallow mixed layer on 28 November might be due to freshwater lens formed by the precipitation. Such observations of thick BLs formed by precipitation are not new. For instance, thick barrier layer (>25 m) formed due to the heavy

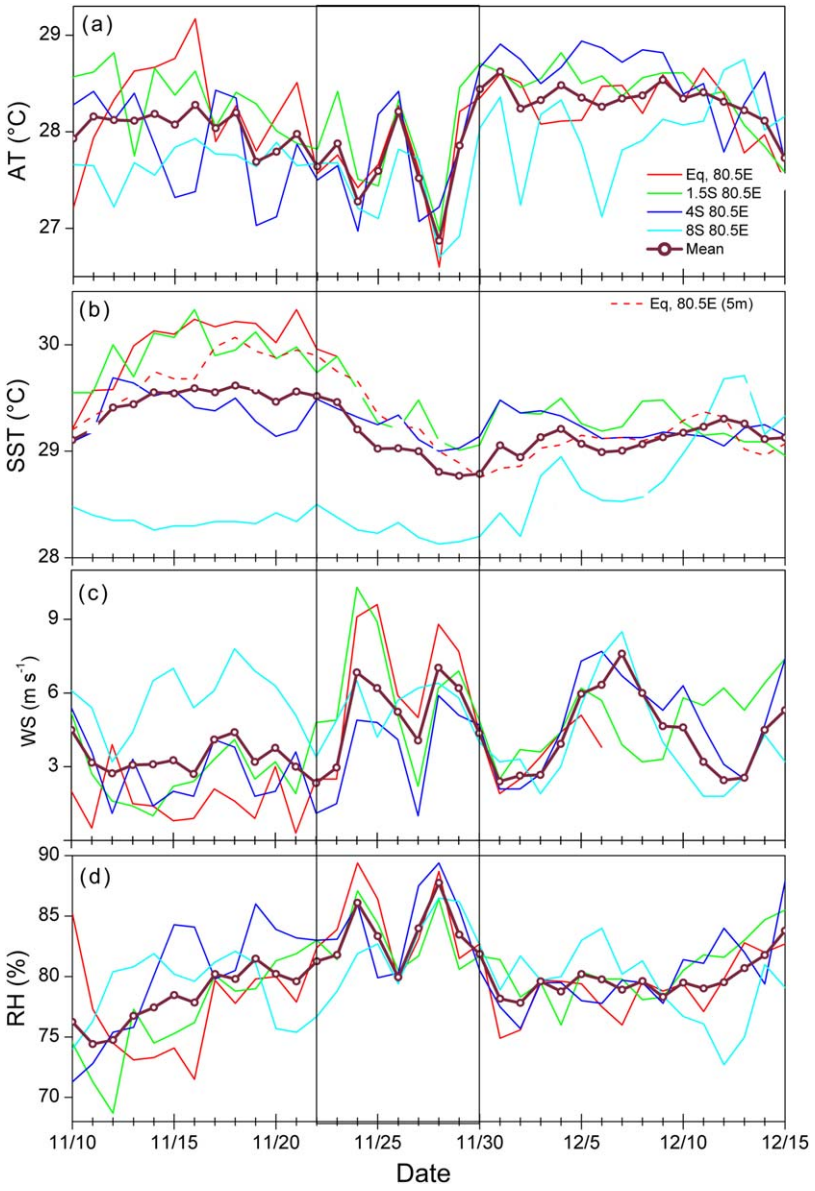

Figure 3. Time series of (a) air temperature, (b) sea surface temperature, (c) wind speed, and (d) relative humidity from RAMA buoys at different latitudes (equator, 1.5°S, 4°S, and 8°S) located along 80.5°E.s

rainfall has been reported from western equatorial Pacific by *Godfrey and Lindstrom* [1989] and *Lukas and Lindstrom* [1991].

The third profile shown in Figure 4c is taken on 26 November, the same day as that of first profile (Figure 4a). But the location of this profile was further east (80.47°E) and very close to equator. Both the profiles were taken within a time difference of ∼2 h and were separated only by ∼600 km. Notable similarity between the profiles in Figures 4a and 4c are their negligibly thin BL. But, in comparison with Figure 4a, the profile in Figure 4c had a deeper (∼67.5 m) mixed layer. However, the isothermal layer (70 m) of third profile was comparable to that in Figure 4b. Strong winds in the active phase of MJO produce such deeper of mixed and isothermal layers [*Lukas and Lindstrom*, 1991]. These examples also display the disparity in the upper ocean thermohaline structure that can be produced by the same MJO event at different locations. It should be noted here that the spatiotemporal difference between the first and third profiles were very small in comparison with the spatial and temporal scale of the MJO. This indicates large heterogeneity of the upper ocean response in the study region during the active phase of MJO. As mentioned before, oceanic

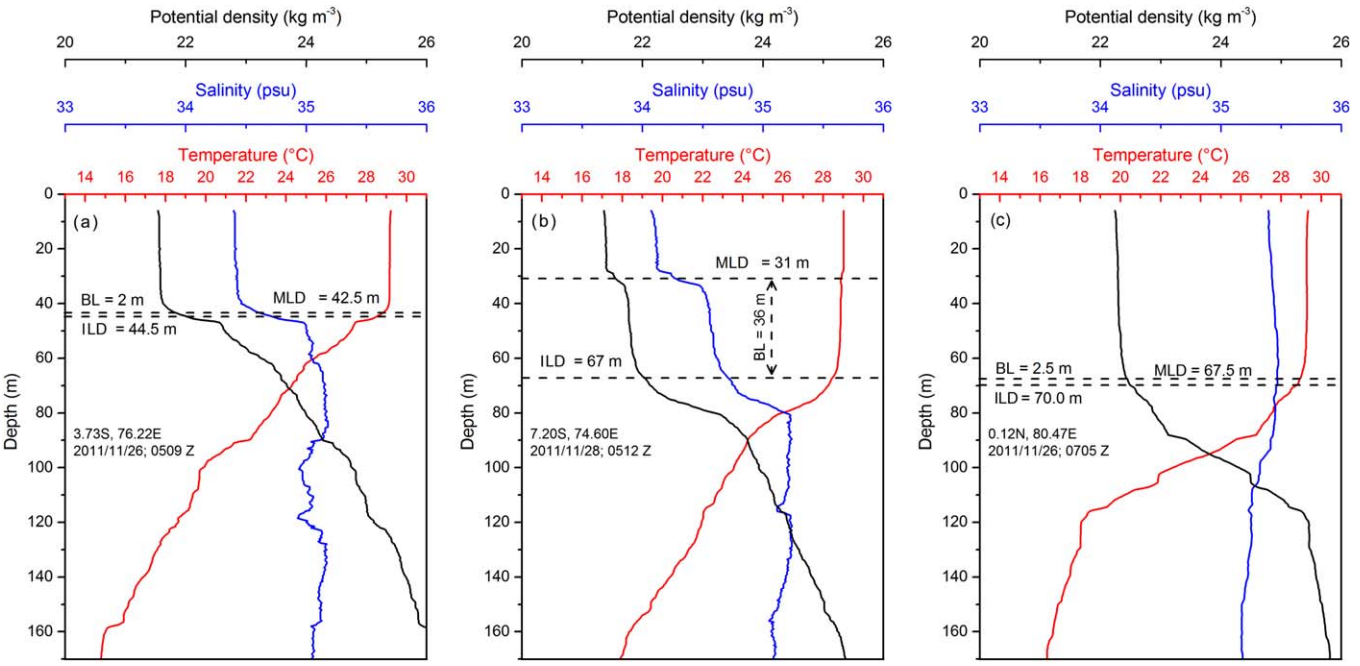

Figure 4. Typical profiles of temperature, salinity, and potential density from AXCTD measurements.

measurements considered here represent the variability from a broad oceanic region. Hence, we initially carried out a statistical analysis of the observations to understand the range of variability in different parameters.

Histograms of MLD during the suppressed and active phase are shown in Figures 5a and 5b. Only 14 good AXCTD profiles were available for the restoring phase. This number was inadequate to produce a meaningful statistics and hence not shown here. In the suppressed phase MLD estimates showed a more or less uniform distribution varied between 25 and 50 m class range, with local minima at 35–40 m bin. On the other hand, the MLD in the active phase had a bimodal distribution (Figure 5b). Sixty-five percent of the MLD estimates were in the 25–45 m shallow mode. The mean MLD in this mode was ∼34 m. Another ∼25% of observed MLD were in the deeper (60–75 m) class range and the mean of this mode was ∼65 m. Table 2 summarizes the statistics of MLD variability. Mixed layer depth is governed by transfer of turbulent fluxes of

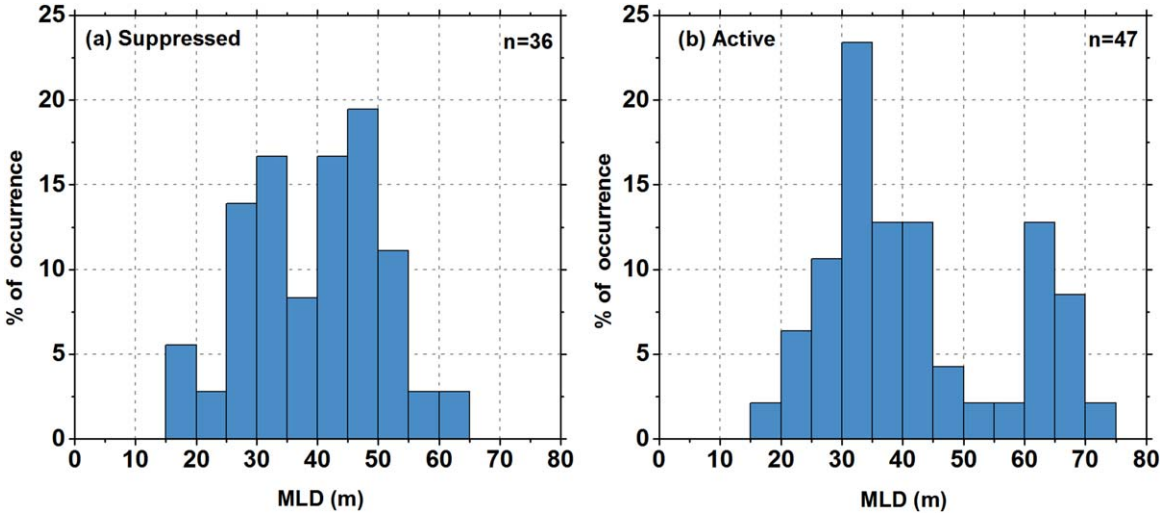

Figure 5. Distribution of mixed layer depth in the (a) suppressed phase and (b) active phase of MJO.

Table 2. Statistics of Ocean Mixed Layer Depth (MLD)

MJO Phase	Number of Profiles	Min (m)	Max (m)	Mean (m)	Std (m)	Mode (m)	Median (m)
Suppressed	36	19	64.5	39.5	11.1	26.0	41.8
Active	47	19	70.5	42.3	15.4	32.5	38.0
Restoring	14	20	58.5	39.3	13.1	44	42.75

heat, mass (freshwater), and momentum across the air-sea interface and the horizontal advection in the ocean surface layer [*Thadathil et al*., 2007]. Because of weak winds and less or little precipitation, heat flux is the dominant factor in determining the MLD in the suppressed phase. The bimodal distribution in the active phase suggests the role of two different processes governing the MLD. While the diabatic cooling and wind stirring during the active phase contribute to the mixed layer deepening [*Drushka et al*., 2012] formation of stable, relatively fresh lenses during the frequent and heavy precipitation during the active phase of MJO produces shallow mixed layers [*Drushka et al*., 2014]. Therefore, the MJO forcing on the upper ocean can lead to contrasting thermohaline structure producing differences in mixed layer characteristics. Such contrasting upper ocean thermohaline structure observed during DYNAMO was already shown in Figure 4. We will further examine the reason for the bimodal distribution later on in this section. Additionally, a discussion on the atmospheric and subsurface processes that give rise to different upper ocean thermohaline behavior is given in section 5. As discussed subsequently, the ILD and D20 distributions too exhibited the bimodal characteristics in the active phase of MJO.

ILD variability was unimodal during the suppressed phase. A large number ($\sim$80%) of observed ILD were in the 25–60 m class range (Figure 6a). A few instances of deeper ($>$80 m) ILD were also present. In contrast, the active phase ILD had the bimodal distribution (Figure 6b). The mode of variability in the 25–55 m class range rather resembled the suppressed phase ILD variability. However, the second mode was in the deeper side of the ILD spectrum, shifted by $\sim$20 to 30 m from the first mode (Figure 6b). Thermocline (as represented by D20) distribution was also bimodal in the active phase (Figure 9b). ILD variability is closely linked to the upward/downward movement of the thermocline [*Thadathil et al*., 2007]. Therefore, it is reasonable to deduce that the observed bimodal distribution of ILD was related to the active phase thermocline variability. In the restoring phase the shape of the ILD histogram was unimodal with peak of the distribution in the 55–65 m class range. Compared to the suppressed phase, a significant percentage of ILD observations were in the deeper ($>$60 m) class ranges during the restoring phase. Moreover, in comparison with suppressed phase, the percentage occurrence of shallow ($<$40 m) ILD was very low in the restoring phase. The range of variability of ILD values during the active phase was comparable to restoring phase. Statistics of variability of the ILD is given in Table 3. Mean ILD in the DYNAMO domain deepened by 19 m during the MJO life cycle. Shallowest and deepest mean ILD were observed in the suppressed (40.0 m) and restoring (59.0 m) phases, respectively.

The variability of BLT in the suppressed and active phases of MJO is shown in Figures 7a and 7b. Regardless of the phase of the MJO around 60% of the occurrence of BLT was in the 0–10 m bin. Observations showed

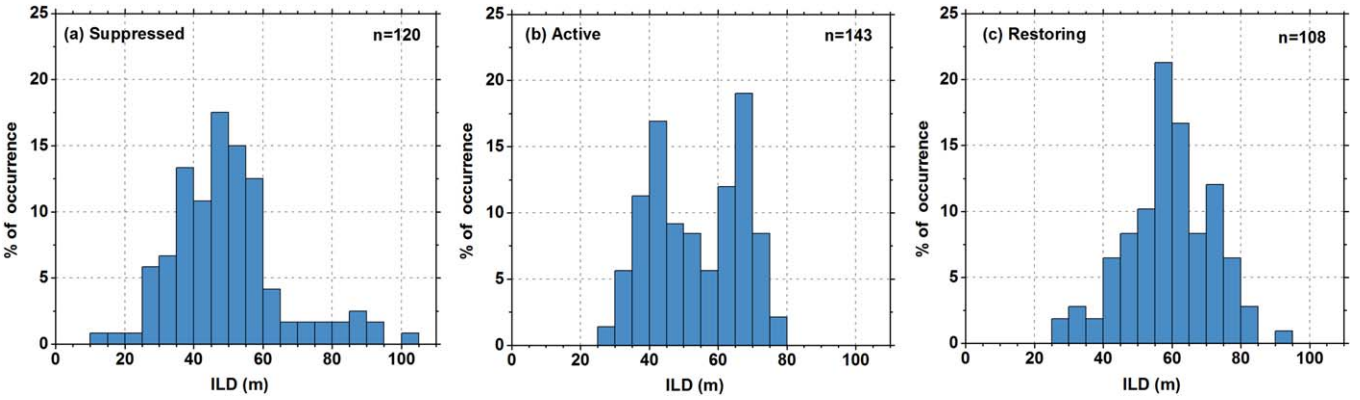

Figure 6. Distribution of isothermal layer depth in the (a) suppressed phase, (b) active phase, and (c) restoring phase of MJO.

Table 3. Statistics of Isothermal Layer Depth (ILD)

MJO Phase	Number of Profiles	Min (m)	Max (m)	Mean (m)	Std (m)	Mode (m)	Median (m)
Suppressed	120	12.5	103.0	40.0	15.9	38.5	48.0
Active	143	29.5	76.0	53.5	13.2	68.5	52.5
Restoring	108	28.0	93	59.0	12.6	51.0	58.8

a very small percentage (∼2%) of thicker (>30 m) BLs formed during the suppressed phase of MJO. Whereas, around 15% of BLs was thicker than 30 m during the active phase. Table 4 summarizes the BLT variability observed in the suppressed and active phase of the MJO. As mentioned in section 4.1, during the active phase of MJO freshwater puddles created by the convective precipitation could produce thick BLs. Figures 8 illustrates such a convection and precipitation event observed on 28 November 2011. Figure 8a is the aircraft-based lower fuselage C-band radar [*Chen et al*., 2016] reflectivity composite of an intense convection observed during 0430Z-0830Z. Band of reflectivity greater than 30–35 dBZ represents the location convection front (CF) during the observation period. Aircraft made observation across and along the CF (dotted line represents the aircraft flight track) and also deployed AXCTDs and AXBTs at different locations. Blue dots in Figure 8a are the positions of 7 AXCTDs launched across the CF to observe the effect of precipitation on the upper ocean stratification.

Longitude-depth cross section of salinity created using the seven AXCTD profiles (positions of which are shown by blue dots in the upper *X* axis of Figure 8b) taken across the CF is shown in Figure 8b. Near surface salinity stratification produced by the freshwater influx in to the ocean is apparent in the cross section. Isohaline of 34.1 psu coincided with the position of CF, which is clear indication of rain induced surface freshening. Moreover, 34.2 psu isohaline deepened up to a depth of 30 m between ∼74.5°E and ∼75°E due to freshening. Interestingly, five out of the seven AXCTD profiles had thick (>30 m) barrier layers. The thickest barrier layer of 48.0 m was exhibited by the AXCTD profile taken right under the CF (fourth profile from east). Mean BLT calculated from the five profiles with deep BL was 43 m.

Distributions of D20 are shown in Figures 9a–9c. During the suppressed phase, the D20 distribution was close to lognormal with the peak in the 100–105 m class. The suppressed phase D20 frequency distribution was highly skewed toward larger values, indicating the occurrence of deeper thermoclines (Figure 9a). Mean D20 during the suppressed phase was 117 m. Active phase D20 exhibited bimodal distribution (Figure 9b). While the primary peak was in the 100–110 m class range, secondary peak was in the 140–150 m class range. Although, distribution of D20 in the active phase was entirely different from that of suppressed phase, mean of D20 was the same in both the phases (Table 5). In fact, deepening of D20 occurred in the restoring phase of the MJO (Figure 9c) with frequency distribution negatively skewed toward smaller values. Additionally, more than half of the D20 observations in the restoring phase was in the narrow class range of

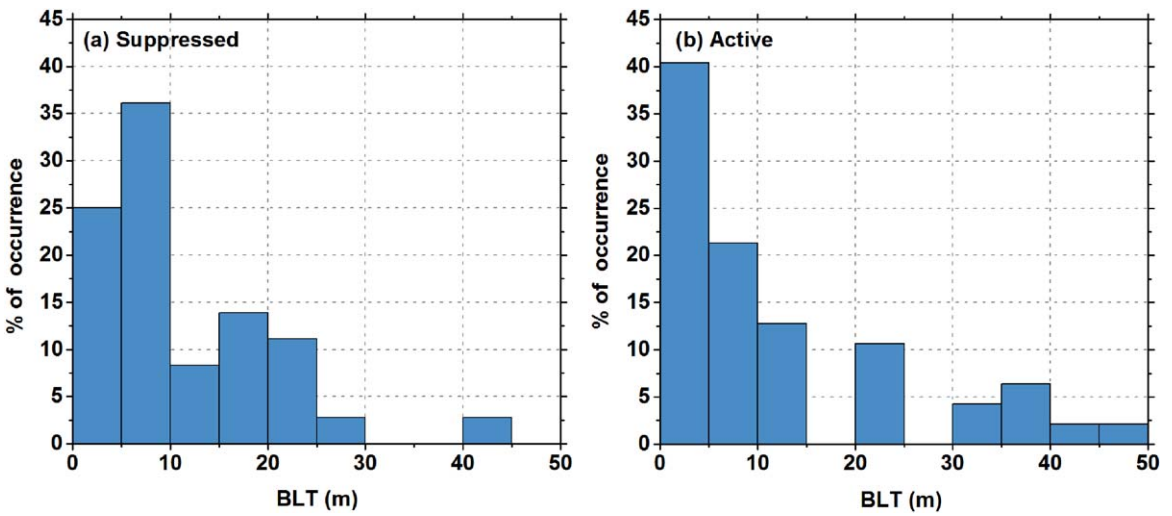

Figure 7. Same as Figure 2, but for barrier layer thickness.

Table 4. Statistics of Barrier Layer Thickness (BLT)

MJO Phase	Number of Profiles	Min (m)	Max (m)	Mean (m)	Std (m)	Mode (m)	Median (m)
Suppressed	36	0.5	40.5	10.7	8.7	2.5	7.5
Active	47	0.5	48.0	12.4	12.9	4.0	6.5
Restoring	14	3.5	37	20	12.1	5	16.5

130–145 m. Mean D20 in the suppressed phase was 130 m which was deeper by 13 m in comparison with suppressed and active MJO phases.

No obvious diurnal variability was present in the MLD, ILD, BL, or D20. However, thermocline showed strong latitudinal variability (Figure 10a), owing to the presence of thermocline ridge in the study region. In general, thermocline was the deepest around 8°S and was the shallowest between 4°S and 2°S during the entire MJO cycle. ILD variability was generally independent of latitude, nonetheless, consistently shallow ILDs tend to occur between 4°S and 2°S than at the other latitudes in the DYANMO domain (Figure 10b). Figure 10c is

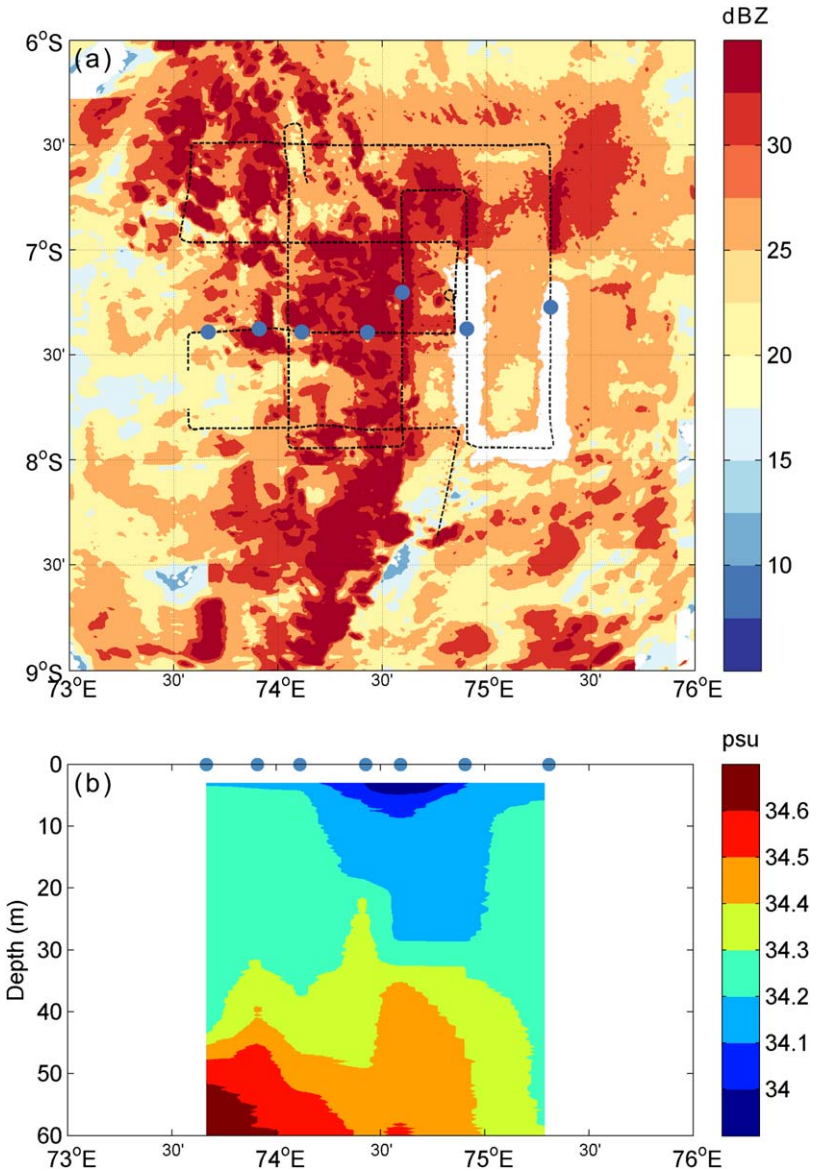

Figure 8. (a) C-band lower fuselage radar reflectivity overlaid with aircraft track in black dashed line. Location of AXCTD profiles are shown in blue dots. (b) Vertical cross section of salinity from AXCTD profiles.

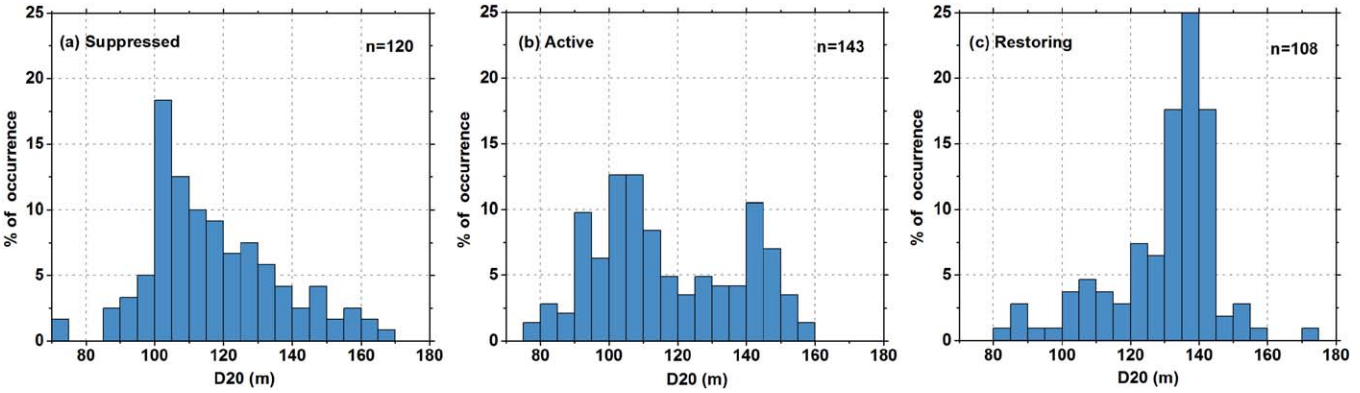

Figure 9. Same as Figure 3, but for thermocline depth as represented by the depth of 20°C isotherm.

the MLD variability with the latitude of observations. No latitudinal dependence was observed in MLD variability.

In the active phase of MJO, deeper thermoclines (>140 m) and isothermal layers (>60 m) were consistently formed between 6°S and 10°S (Figure 10a). OLR anomaly shown in Figure 2 indicates strong MJO activity in this latitude range for a few days in the in the active phase. Here the magnitude of OLR anomaly often exceeded 100 W m^{-2}. Therefore, the influence of active MJO cannot be ruled out for the formation of deeper D20 and ILD. We found that, these observations from south of 6°S were responsible for the active phase secondary peak in D20 distribution (Figure 9). Meanwhile, the secondary peak in the ILD distribution (Figure 6) additionally consisted of near equator (north of 1°S) observations too. Figure 10b shows significant fluctuation in ILD near the equator during active phase. ILD varied from ∼30 to ∼75 m here. Moreover, about half of these near equator observations were in the deeper ILD category (>60 m). Therefore, unlike the D20, the deeper mode of ILD distribution in the active phase was the combined effect of ILD deepening observed at south of 6°S and north of 1°N. Similar to isothermal layer, MLD also showed considerable variability near the equator. MLD varied from ∼20 to ∼70 m during the active phase of MJO. The secondary peak in Figure 5 consisting of deeper mixed layers was due to the near equator deep MLD (>60 m) observations. ILD and MLD fluctuation observed near the equator might be due to the spatial and temporal differences in the impact of MJO on the upper ocean. We will discuss more about the upper ocean evolution under the influence of the MJO activity in section 5.

Distributions of SST (estimated by averaging top 3 m of temperature profile) during the suppressed, active, and restoring phases are shown in Figures 11a–11c. Active phase SST distribution was notably different from other two phases. Variance of SST in active MJO phase was very low in comparison with the suppressed and restoring periods of MJO. Also, approximately 60% of active phase SST observations were in the narrow class range of 29–29.4°C. Standard deviation of SST was only 0.2°C in the active phase, whereas in the suppressed and restoring phase it was 0.5°C. Moreover, the sea surface cooled by ∼0.5°C in the DYNAMO domain by the passage of MJO (Table 6).

4.2. Characteristics of Water Column During the Active MJO

Vertical cross section of temperature, salinity, and density between DG and RV across the DYNAMO southern domain (see Figure 1) is shown in Figure 12. Lower and upper *X* axes represents, respectively, the distance from DG and corresponding latitudes. Thirteen AXBT and six AXCTD profiles were used to construct the cross sections. Black (white) dotted lines represent the distance of AXBT (AXCTD) profiles from DG. Measurements were started at 0405 UTC on 26 November (in the active phase of MJO) from DG and

Table 5. Statistics of Thermocline Depth (D20)

MJO Phase	Number of Profiles	Min (m)	Max (m)	Mean (m)	Std (m)	Mode (m)	Median (m)
Suppressed	120	71.8	166.7	117.0	18.9	92.5	112.4
Active	143	76.4	156.6	117.0	20.7	104.0	110.6
Restoring	108	83.3	172.6	130.0	15.8	134.1	172.6

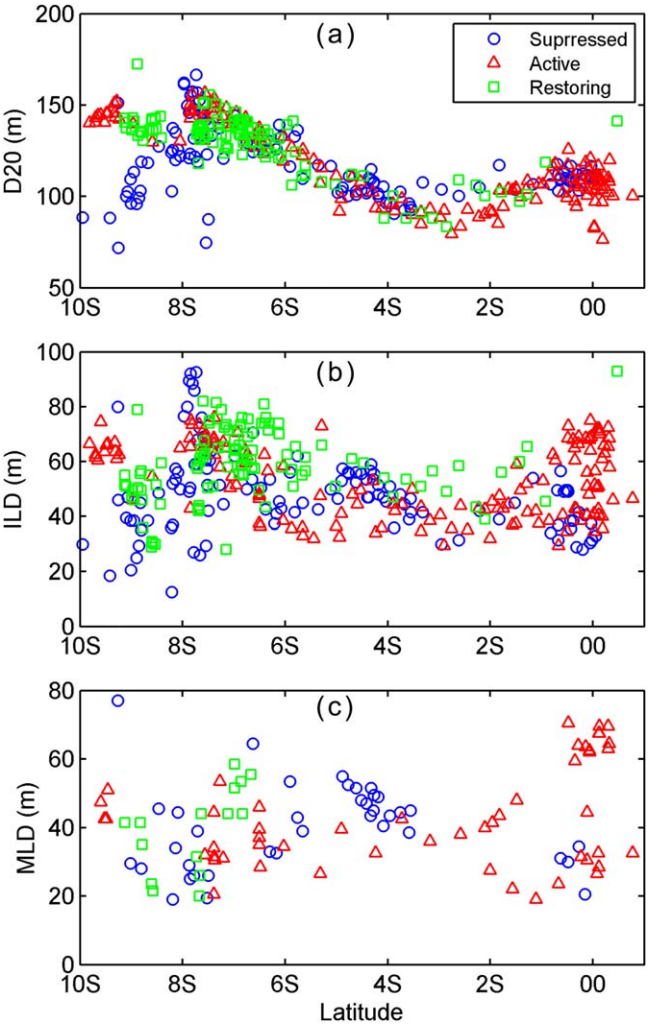

Figure 10. Latitudinal variability of (a) thermocline depth and (b) isothermal layer depth.

continued for 2.5 h. Near surface temperature was higher than 29°C almost everywhere (Figure 12a). Thermocline region showed a distinct bow structure. Thermocline was shallower between ~4°S (440 km) and ~2°S (~900 km) and deepened toward DG and RV sides. As mentioned before (Figure 10a), this particular structure of the thermocline was due to the SCTR.

Vertical cross sections of salinity and potential density were created only using the AXCTD profiles (Figures 12b and 12c). The white vertical stripes in the figures are the data gaps where no salinity data was available for adequate interpolation. Near DG, surface salinity was lower by ~1 psu in comparison with that at RV. It can be seen that 35 psu isohaline (shown by thicker contour line) is deeper (~90 m) near DG and steadily shoaled toward equator. Near RV (~1.28°S), the 35 psu isohaline shoaled to the surface level. Also there existed a subsurface salinity maximum nearby RV with salinity higher than 35.4 psu between 20 and 100 m with high salinity core located around 80 m. Latitudinal variability of sea surface salinity observed in the AXCTD data agreed well with Aquarius satellite observation (not shown). This observed water column salinity variability was attributed to the different water masses present in the DYNAMO domain. Similar to temperature, density also showed the distinct bow structure. However, as noticeable from the 22 kg m^{-3} isopycnal, near-surface density was more analogous to the

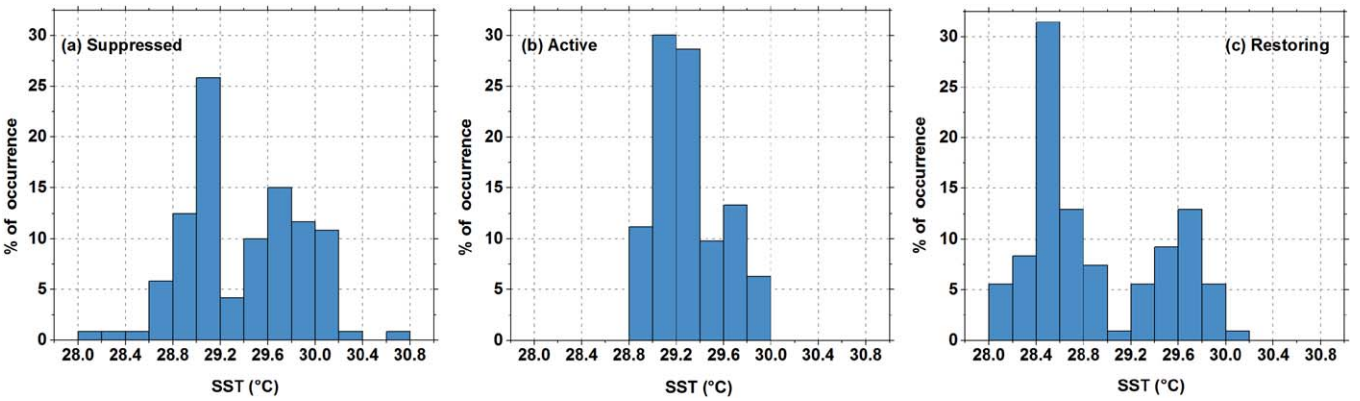

Figure 11. Same as Figure 5, but for sea surface temperature.

Table 6. Statistics of Sea Surface Temperature (SST)

MJO Phase	Number of Profiles	Min (°C)	Max (°C)	Mean (°C)	Std (°C)	Mode (°C)	Median (°C)
Suppressed	120	28.1	30.6	29.4	0.5	28.7	29.4
Active	143	28.8	29.9	29.3	0.2	28.9	29.3
Restoring	108	28.1	30.1	28.9	0.5	28.1	28.7

variability of salinity. This indicates that density variability at the surface and subsurface was determined, respectively, by the salinity and temperature.

Figure 13a shows the T-S diagram of the AXCTD profile nearest to DG; the southernmost of the six AXCTD profiles (same AXCTD profiles used in Figure 12). Contours in the figure represent the constant potential density surfaces. From the T-S diagram the Indonesian through flow (ITF) water can be identified as the isohaline (∼35 psu) layer that present between potential densities 23.5 and 25.5 kg m^{-3} [*Song et al*., 2004; *New et al*., 2007]. Surface water in this region was dominated by fresher tropical surface water (TSW) with a lower salinity than ITF water [*Jensen*, 2003, 2001]. TSW was also observed in the surface waters of the next three profiles shown in Figure 13b. Toward RV, the isohaline character of ITF is disturbed by the higher salinity water at lower latitudes. High salinity water intrusion into subsurface layers with a high salinity core at 80 m is also apparent in the vertical cross section of salinity, between 400 and 800 km from DG (Figure 12b). This intrusion increases with decreasing latitude as seen from the red curve in Figure 13b with slightly higher salinity than other two plots. The source of this high salinity core is the Arabian Sea high saline water (ASHW). Characteristic temperature of this water is between 28 and 24°C with salinity between 36.7 and 35.3 psu and potential density varies from 22.8 to 24.5 kg m^{-3} [*Sardessai et al*., 2010; *Kumar and Prasad*, 1999]. ASHSW completely replaced the ITF in the two northernmost profiles closest to RV shown in Figure 13c. In comparison with the other profiles at higher latitudes, the surface water of these two profiles had different characteristic than that of TSW. Here the surface salinity was in between fresh TSW and high saline ASHSW. This was a mixture of Bay of Bengal (BoB) water and ITF [*Sardessai et al*., 2010; *Sengupta et al*., 2006].

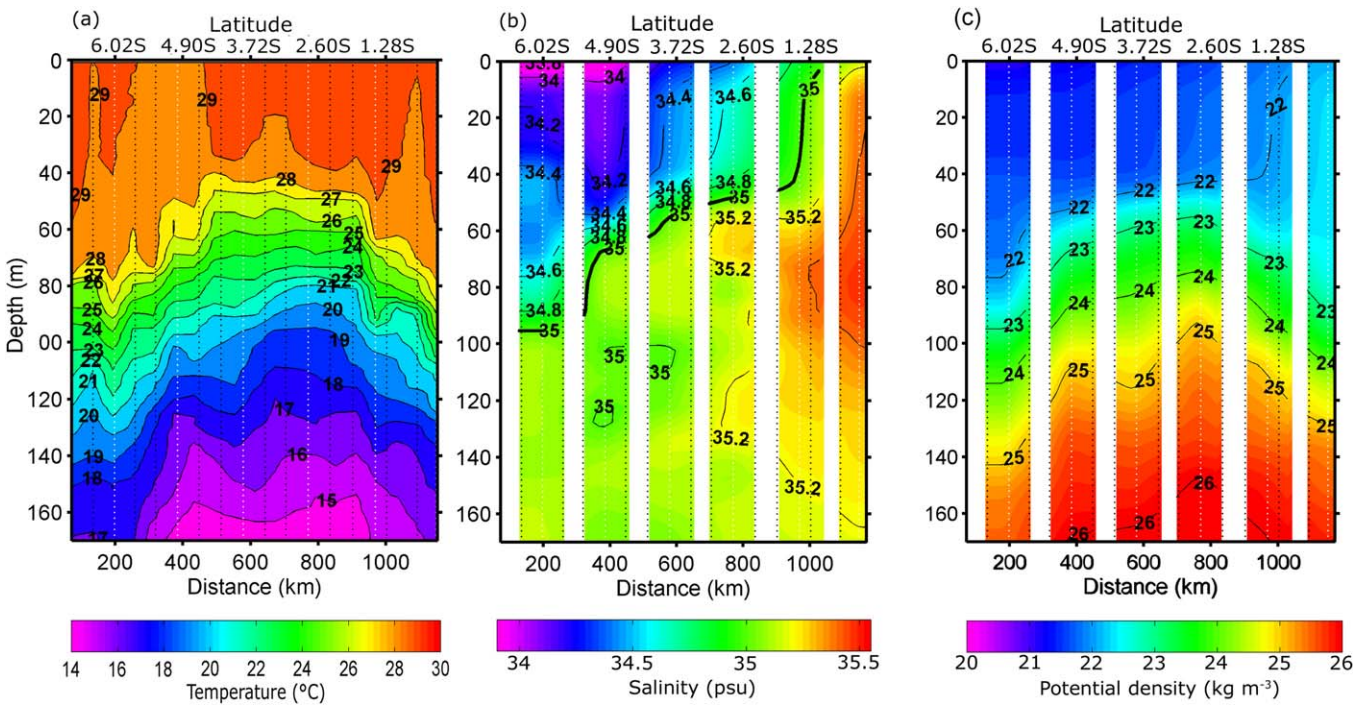

Figure 12. Vertical cross section of temperature along the diagonal transect from Diego Garcia to R/V Revelle. (a) Water temperature, (b) salinity, and (c) potential density. The origin of the horizontal axis is at Diego Garcia.

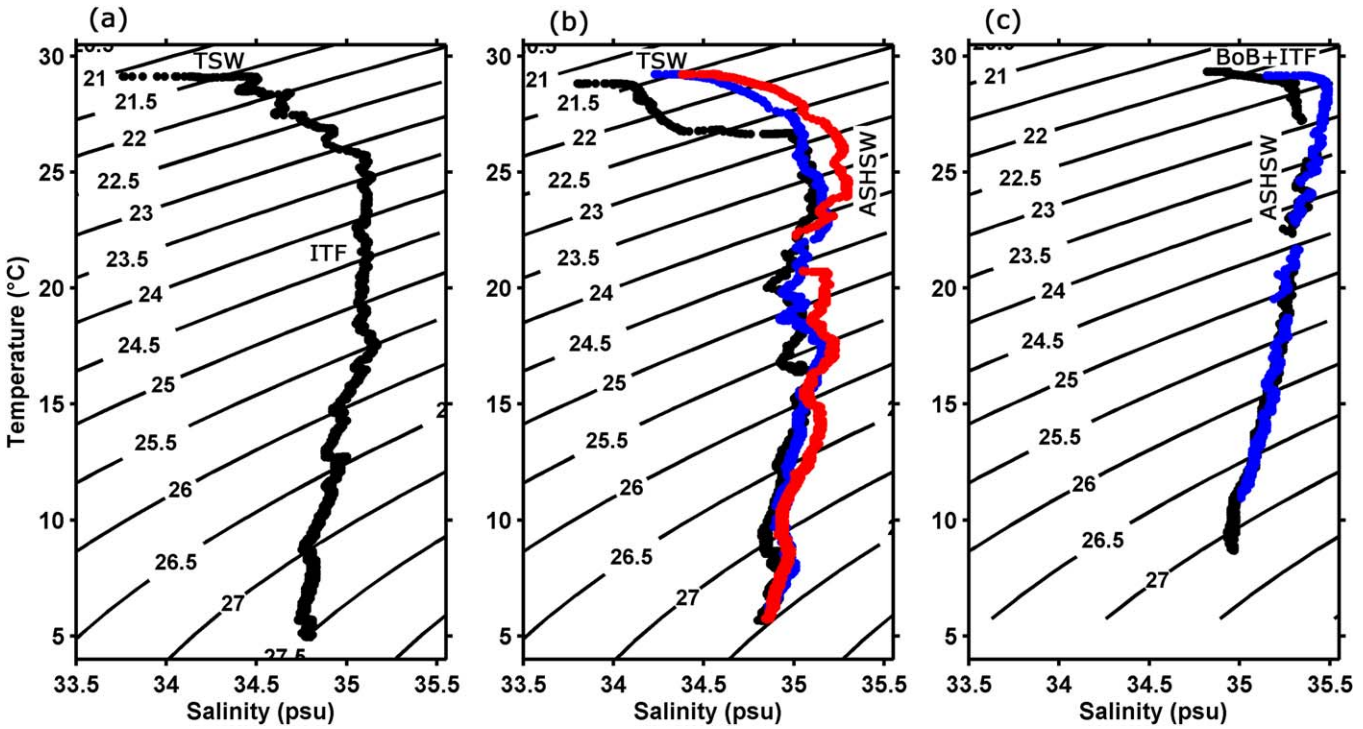

Figure 13. T-S diagrams of AXCTD profiles used in Figure 9. (a) Southernmost profile 200 km from Diego Garica. (b) Profiles 400 km (black), 600 km (blue) and 800 km (red) from Diego Garica. (c) Profile 1000 km from Diego Garica (black) and near RV Revelle (blue).

5. Upper Ocean Variability Observed in RAMA Buoy Data

The analysis presented here depicted the gamut of variability observed in various parameters that defines the upper ocean thermohaline structure when forced by an intense MJO. It is known that the impact of MJOs on the upper ocean can be substantially vary from event to event [*Drushka et al*., 2014]. Differences in the strength and timing of convection, wind, and precipitation as well as the subsurface stratification all affect the response of upper ocean [*Drushka et al*., 2014]. Similarly, it is also possible that a particular MJO event can produce contrasting upper ocean response at different locations even separated by small distance (compared with very large spatial scale of MJO). Upper ocean profiles (Figures 4a and 4c) discussed in section 4.1 were examples for such observations made during DYNAMO. Additionally, the bimodal distribution of MLD (Figure 5b) also suggests nonuniform upper ocean response in the active phase of MJO. To understand this aspect in detail, we examined the evolution of upper ocean thermohaline structure during DYNAMO in the different phases of the MJO. Time series data from two RAMA buoys located at 80.5°E and 90°E along equator moored in the study domain were considered for the analysis.

Figure 14 shows the comparison of wind, precipitation, and subsurface variability observed at the buoys during the MJO cycle. Even though distance between the buoys (9.5°) was very small compared with planetary spatial scale of MJO the ocean variability induced by MJO at the two locations were significantly different. For instance, at 80.5°E increase in zonal wind speed associated with active MJO occurred on 23 November and reduced soon after active phase of MJO (Figure 14a). Whereas at 90°E the zonal wind was weak until 27 November then increased abruptly (Figure 14f) and strong winds maintained even after the end of active phase of MJO. In addition to zonal wind, precipitation pattern (Figures 14b and 14g) was also considerably different at two locations. Figure 14b indicates significant convection at 80.5°E even before the onset of MJO and continued through the active phase. Here abrupt shutdown of convection occurred toward the end of active phase. On the contrary, convection intensified at 90°E toward the end of the active phase and continued for a few more days after the active MJO period (Figure 14g). In this atmospheric scenario, upper ocean stratification evolved differently at 80.5°E and 90°E during MJO cycle.

The tandem variability of MLD (solid line) and ILD (dotted line) at 80.5°E indicates that the upper ocean stratification during the suppressed and active phase of MJO was chiefly governed by temperature (Figure

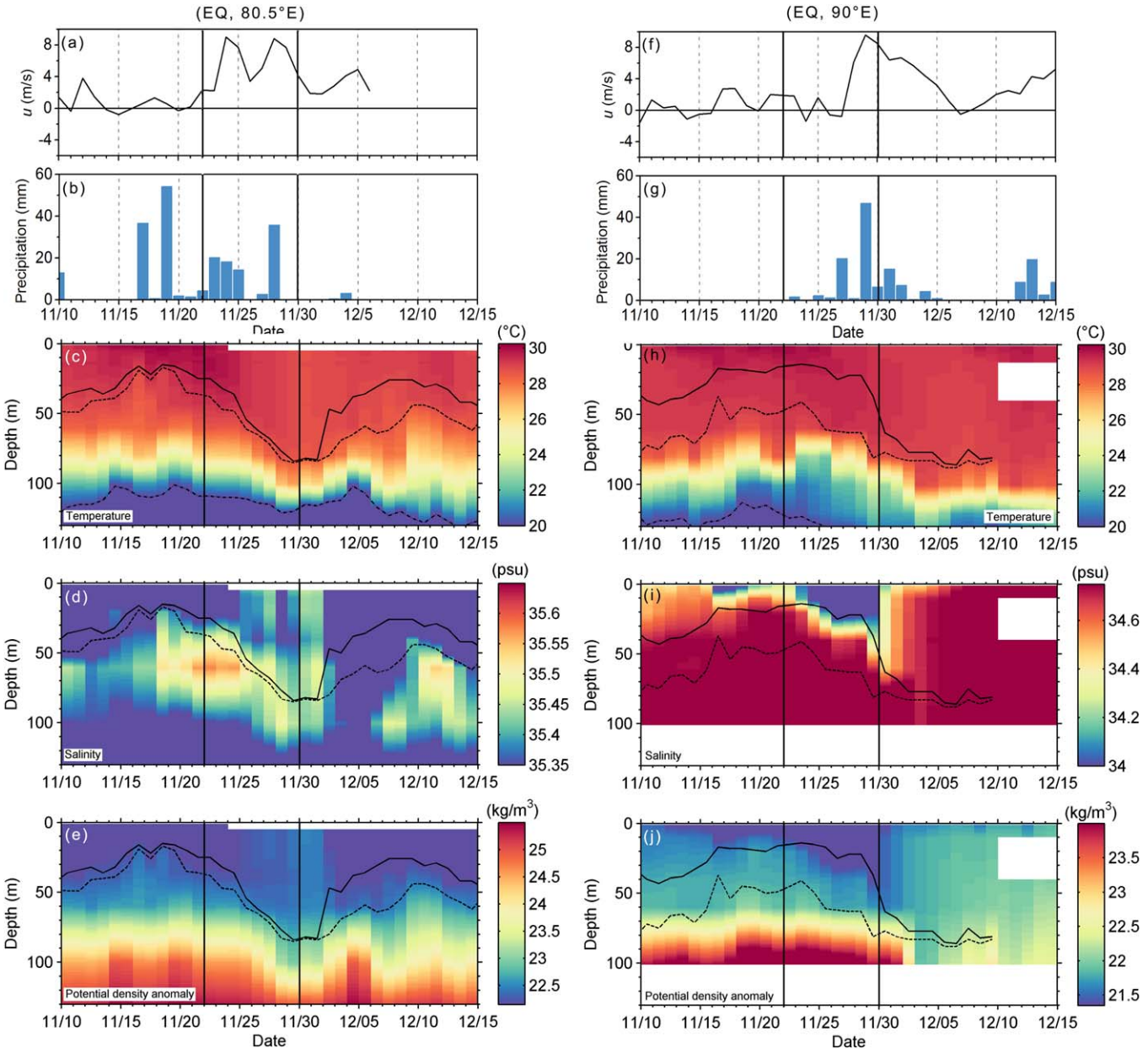

Figure 14. Time series of (a) zonal wind, (b) precipitation as well as time-depth cross sections of (c) water temperature, (d) salinity, and (e) potential density at buoy location (Eq, 80.5°E). Figures (f–j) are same as figures (a–e) but for the buoy locations (Eq, 90°E). MLD (solid line), ILD (dotted line), and D20 (dashed line) are also shown in the cross sections.

14c) and hence a thin BL. Moreover, low winds (Figure 14a) and the subsurface salinity maximum centered around 60 m depth (Figure 14d) produced relatively shallow MLD and ILD. However, strong wind induced mixing in the active phase of MJO caused the deepening of mixed layer. Later in the active phase, deepening of ML and mixing brought the subsurface high saline water into the mixed layer to produce more or less uniform salinity from surface up to ~100 m depth. Also, this eroded the previously existing thin BL. Possible reason for the thickening BL in the restoring phase is the decrease in wind speed and absence of subsurface salinity maximum for a brief period after the active phase.

Meanwhile, at 90.5°E thick BL persisted from the beginning of suppressed phase through the active phase, indicating the strong upper ocean salinity stratification (Figure 14h). Late intensification of wind at 90.5°E and hence less mixing, helped to maintain the BL throughout in the active phase. The role of surface

freshening (near surface salinity minimum) by the precipitation also cannot be ruled out for the maintenance of thick BLs in the active phase (Figure 14i).

Thermohaline characteristics at the two RAMA buoy sites analyzed here evolved differently during the active phase of MJO. While the mixed layer deepened from ~35 to ~85 m at 80.5°E, it remained shallow (~30 m) at 90°E. Evolution of isothermal layer and thermocline at the two sites were also dissimilar in the active phase. This demonstrates how the differences in the strength and timing of convection, wind, and precipitation as well as the subsurface stratification modulate the upper ocean thermohaline structure during a MJO event. Hence, it would be reasonable to infer that the bimodal characteristics of distributions observed in the active phase are produced by the heterogeneity in the upper ocean response in the study region. This also emphasizes the need of making domain wide in situ measurements to investigate the statistical variability produced by a MJO.

6. Discussion and Summary

Atmospheric perturbations associated with MJO have profound impact on the upper ocean thermohaline structure and variability. Reduction in incoming solar radiation, precipitation produced freshwater influx in to the ocean surface, and strong surface winds during the active phase of MJO modify ocean mixed layer dynamics. One of the earliest observational studies on the MJO's influence on the ocean mixed layer is by *Lukas and Lindstrom* [1991] using the data collected from western Pacific Ocean. They reported significant (~22 m) deepening of mixed layer in the strong wind and convective (active) phase of MJO. Subsequently, model simulations also confirmed similar MJO associated MLD variability in the Indo-Pacific region [e.g., *Shinoda and Hendon*, 1998; *Waliser et al*., 2003]. *Drushka et al*. [2012] found that the composite MJO anomalies of the MLD exhibited systematic variations in the Indian Ocean with amplitudes up to ±10 m. While the surface warming and light winds during the suppressed phase cause the mixed layer to shoal the deepening of mixed layer in the active MJO phase was attributed to the diabatic cooling and wind stirring.

Statistics of MLD variability presented in this paper (Table 2) gives an impression that the mixed layer deepening during DYNAMO was insignificant. Our observations show that, on an average mixed layer deepened only by 2.8 m in the active phase of MJO, which is too low in comparison with previous reports. Nonetheless, this does not mean that deepening of mixed layer did not occur anywhere in the DYNAMO domain during this particular MJO event. As shown in the Figure 5b, MLD distribution during the active phase had a secondary mode in the deeper side of the MLD spectrum. Mean of this mode was ~65 m, which is ~25.5 m deeper than the average suppressed phase MLD, and this value matches fairly well with the previous observation by *Lukas and Lindstrom* [1991] mentioned above. Therefore, it is reasonable to infer that mixed layer response to the active phase of MJO was not similar everywhere in the DYNAMO domain. This fact is also indicated by the higher MLD standard deviation (15.4 m) during the active phase MLD in comparison with suppressed phase (11.1 m). RAMA buoy observations too support these findings. Figure 15 depicts the time evolution of MLD at RAMA buoy sites at three different latitudes located along 80.5°E. At the equator, the MJO-related MLD variability was very obvious with an average deepening of ~30 m in the active phase. However, at the other two locations the MLD variability seemed to be influenced little by the MJO. As mentioned before, the bimodal distribution of MLD observed in the active phase can be attributed to this non uniform response of upper ocean in the DYNAMO domain.

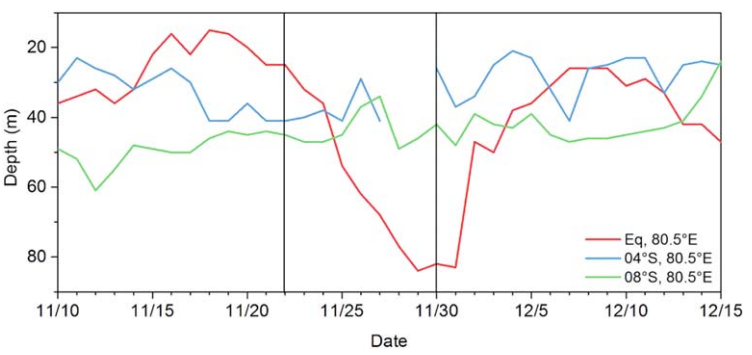

Figure 15. Mixed layer depth evolution at three different RAMA buoy locations.

We also noticed that shallow mixed layers formed in the freshwater lenses produced by heavy precipitation events during the MJO active phase. Associated with this thick (>30 m) barrier layers often formed under the freshwater puddles. However, it is known that preexisting or newly formed BLs erodes

immediately during the active phase of MJO due to the wind stirring and convective mixing from the surface cooling [*Zhang and McPhaden*, 2000; *Cronin and McPhaden*, 2002]. Furthermore, the local precipitation formed rain water puddles tend to produce considerably thinner (~10 m) BLs [*You*, 1995; *Vialard and Delecluse*, 1998] than those observed in the present study. Therefore, the thick BLs observed during the precipitation event reported here is intriguing. Unfortunately, we do not have the information on the life time of these BLs since the aircraft could not make repeated sorties in the same area due to flight time limitations. However, *You* [1995] and *Cronin and McPhaden* [2002] have demonstrated that the thick barrier layers can exist for considerably long period of time even during westerly wind bursts. These BLs were indeed not produced by the rain alone. Advection of freshwater (likely produced by persistent storm rains) in the upper level over the high salinity water in the bottom moving in the opposite direction produces ideal condition for the existence of thick BLs [*You*, 1995; *Cronin* and *McPhaden*, 2002]. Further analysis of AXCTD data along with Aquarius satellite derived ocean surface salinity and RAMA buoy current data is planned to examine the role of such advection processes for the production thick BLs.

SCTR straddled in the DYNAMO domain produced relatively shallow thermocline. South of ~3°S thermocline showed notable positive latitudinal gradient (Figure 10a). Here the thermocline deepened by an average of 8.3 m per latitude. The role of westward propagating annual oceanic Rossby wave (centered around 12°S) cannot be ruled out for producing deeper thermoclines in the higher latitudes of study region [*Périgaud and Delecluse*, 1992; *Fu and Smith*, 1996]. It has already been reported that, downwelling Rossby waves in the southern latitudes of SCTR reduce the upwelling by deepening the thermocline [*Xie et al*., 2002]. In addition to this, *Sieki et al*. [2013] has reported that during the DYNAMO period, a region of positive sea level anomaly propagated westward from 90°E to 70°E, centered at 10°S with a phase speed of 0.2 m/s corresponding to annual downwelling oceanic Rossby wave. Our examination of Aviso mean sea level anomaly data showed the northward extension of this positive sea level anomaly (>15 cm) was up to 4°S during DYNAMO (not shown).

In addition to these we also carried out the water mass analysis based on T-S diagrams, which elucidated different water masses that constitute surface and subsurface waters of DYNAMO domain in the active phase of MJO. This brought out a variety of different water masses present in the subsurface and surface. For instance, subsurface water was chiefly consists of ITF water in the higher latitudes of study region, however, intrusion of ASHSW in to the subsurface from equatorial region was also observed in the DYNAMO domain. Core of the ASHSW (characterized by its higher salinity than ITF water) was centered at a depth of 80 m. Meanwhile, the surface waters were dominated by TSW and a mixture of Bay of Bengal and ITF waters.

Furthermore, an examination of the evolution of upper ocean thermohaline structure based on data from two RAMA buoy sites (80.5°E and 90°E along equator) were also carried out. This showed that the upper ocean response to the MJO forcing at different sites separated even by small distance (compared with planetary spatial scale of MJO) can vary significantly. In short, this analysis, first of its kind from the data sparse and climatically important southern tropical Indian Ocean, provides a broad and clear picture of upper ocean response as well as the variability of thermohaline structure in different phases of MJO.

Acknowledgments

This work was supported by ONR award N0001413WX20025 and partly by NSF award AGS1062300. Denny P. Alappattu was sponsored by the National Research Council research associate ship program. AXCTD and AXBT data used for this study are available at http://data.eol.ucar.edu/master_list/?project=DYNAMO. Outgoing longwave radiation data can be downloaded from http://www.esrl.noaa.gov/psd/. Research moored array for African-Asian-Australian monsoon analysis and prediction (RAMA) buoy data are available from http://www.pmel.noaa.gov/.

References

Alappattu, D. P., and Q. Wang (2015), Correction of depth bias in upper ocean temperature and salinity profiling measurements from airborne expendable probes, *J. Atmos. Oceanic Technol.*, *32*, 247–255.

Argo (2000), Argo float data and metadata from Global Data Assembly Centre (Argo GDAC), SEANOE. [Available at http://doi.org/10.17882/42182.]

Cassou. C. (2008), Intraseasonal interaction between the Madden-Julian Oscillation and the North Atlantic Oscillation, *Nature*, *455*, 523–527.

Chen, S., B. Kerns, N. Guy, D. Jorgensen, J. Delanoë, N. Viltard, C. Zappa, F. Judt, C. Lee, and A. Savarin (2016), Aircraft observations of dry air, ITCZ, convective cloud systems and cold pools in MJO during DYNAMO, *Bull. Am. Meteorol. Soc.*, *97*, 405–423, doi:10.1175/BAMS-D-13-00196.1.

Cronin, M. F., and M. J. McPhaden (1997), The upper ocean heat balance in the western equatorial Pacific warm pool during September-December 1992, *J. Geophys. Res.*, *102*(C4), 8533–8553, doi:10.1029/97JC00020.

Cronin, M. F., and M. J. McPhaden (2002), Barrier layer formation during westerly wind bursts, *J. Geophys. Res.*, *107*(C12), 8020, doi:10.1029/2001JC001171.

DeMott, C. A., N. P. Klingaman, and S. J. Woolnough (2015), Atmosphere-ocean coupled processes in the Madden-Julian oscillation, *Rev. Geophys.*, *53*, 1099–1154, doi:10.1002/2014RG000478.

Drushka, K., J. Sprintall, S. T. Gille, and S. Wijffels (2012), In situ observations of Madden-Julian oscillation mixed layer dynamics in the Indian and Western Pacific Oceans, *J. Clim.*, *25*, 2306–2328.

Drushka, K., J. Sprintall, and S. T. Gille (2014), Subseasonal variations in salinity and barrier-layer thickness in the eastern equatorial Indian Ocean, *J. Geophys. Res. Oceans*, *119*, 805–823, doi:10.1002/2013JC009422.

Duvel, J. P., R. Roca, and J. Vialard (2004), Ocean mixed layer temperature variations induced by intraseasonal convective perturbations over the Indian Ocean, *J. Atmos. Sci.*, *61*, 1004–1023.
Flatau, M., and Y.-J. Kim (2013), Interaction between the MJO and Polar Circulations, *J. Clim.*, *26*, 3562–3574.
Foltz, G. R., J. Vialard, B. Praveen Kumar, and M. J. McPhaden (2010), Seasonal mixed layer heat balance of the Southwestern Tropical Indian Ocean, *J. Clim.*, *23*, 947–965.
Fu, L.-L., and R. D. Smith (1996), Global ocean circulation from satellite altimetry and high-resolution computer simulation, *Bull. Am. Meteorol. Soc.*, *77*(11), 2625–2636.
Girishkumar, M. S., M. Ravichandran, M. J. McPhaden, and R. R. Rao (2011), Intraseasonal variability in barrier layer thickness in the south central Bay of Bengal, *J. Geophys. Res.*, *116*, C03009, doi:10.1029/2010JC006657.
Godfrey, J. S., and E. J. Lindstrom (1989), The heat budget of the equatorial western Pacific surface mixed layer, *J. Geophys. Res.*, *94*(C6), 8007–8017, doi:10.1029/JC094iC06p08007.
Gottschalck, J., P. E. Roundy, C. J. Schreck III, A. Vintzileos, and C. Zhang (2013), Large-scale atmospheric and oceanic conditions during the 2011–12 DYNAMO field campaign, *Mon. Weather Rev.*, *141*, 4173–4196.
Han, W., T. Shinoda, L.-L. Fu, and J. P. McCreary (2006), Impact of atmospheric intraseasonal oscillations on the Indian Ocean dipole during the 1990s, *J. Phys. Oceanogr.*, *36*, 670–690.
Harrison, D. E., and G. A. Vecchi (2001), January 1999 Indian Ocean cooling event, *Geophys. Res. Lett.*, *28*, 3717–3720, doi:10.1029/2001GL013506.
Hendon, H. H., and J. Glick (1997), Intraseasonal air-sea interaction in the tropical Indian and Pacific Oceans, *J. Clim.*, *10*, 647–661.
Hendon, H. H., M. C. Wheeler, and C. Zhang (2007), Seasonal dependence of the MJO-ENSO relationship, *J. Clim.*, *20*, 531–543.
Hermes, J. C., and C. J. C. Reason (2008), Annual cycle of the South Indian Ocean (Seychelles-Chagos) thermocline ridge in a regional ocean model, *J. Geophys. Res.*, *113*, C04035, doi:10.1029/2007JC004363.
Jensen, T. G. (2001), Arabian Sea and Bay of Bengal exchange of salt and tracers in an ocean model, *Geophys. Res. Lett.*, *28*, 3967–3970.
Jensen, T. G. (2003), Cross-equatorial pathways of salt and tracers from the northern Indian Ocean: Modelling results, *Deep Sea Res., Part II*, *50*, 2111–2128
Jiang, X., et al. (2015), Vertical structure and physical processes of the Madden-Julian oscillation: Exploring key model physics in climate simulations, *J. Geophys. Res. Atmos.*, *120*, 4718–4748, doi:10.1002/2014JD022375.
Johnson, R. H., and P. E. Ciesielski (2013), Structure and properties of Madden-Julian Oscillations deduced from DYNAMO sounding arrays, *J. Atmos. Sci.*, *70*, 3157–3179, doi:10.1175/JAS-D-13-065.1.
Kumar, S. P., and T. G. Prasad (1999), Formation and spreading of Arabian Sea high-salinity water mass, *J. Geophys. Res.*, *104*(C1), 1455–1464, doi:10.1029/1998JC900022.
Levitus, S., J. I. Antonov, T. P. Boyer, R. A. Locarnini, H. E. Garcia, and A. V. Mishonov (2009), Global ocean heat content 1955–2008 in light of recently revealed instrumentation problems, *Geophys. Res. Lett.*, *36*, L07608, doi:10.1029/2008GL037155.
Liebmann, B., and C. A. Smith (1996), Description of a complete (interpolated) outgoing longwave radiation dataset, *Bull. Am. Meteorol. Soc.*, *77*, 1275–1277.
Lin, J. L., et al. (2006), Tropical intraseasonal variability in 14 IPCC AR4 climate models. Part I: Convective signals, *J. Clim.*, *19*, 2665–2690.
Lukas, R., and E. Lindstrom (1991), The mixed layer of the western equatorial Pacific Ocean, *J. Geophys. Res.*, *96*(S01), 3343–3357, doi:10.1029/90JC01951.
Madden, R. A., and P. R. Julian (1972), Description of global-scale circulation cells in the tropics with a 40–50 day period, *J. Atmos. Sci.*, *29*, 1109–1123.
Matthews, A. J., P. Singhruck, and K. J. Heywood (2010), Ocean temperature and salinity components of the Madden-Julian oscillation observed by Argo floats, *Clim. Dyn.*, *35*(7), 1149–1168, doi:10.1007/s00382-009-0631-7.
Moum, J., et al. (2014), Air-sea interactions from westerly wind bursts during the November 2011 MJO in the Indian Ocean, *Bull. Am. Meteorol. Soc.*, *95*(8), 1185–1199.
New, A. L., S. G. Alderson, D. A. Smeed, and K. L. Stansfield (2007), On the circulation of water masses across the Mascarene Plateau in the South Indian Ocean, *Deep Sea Res., Part I*, *54*, 42–74, doi:10.1016/j.dsr.2006.08.016.
Pai, D. S., Jyoti Bhate, O. P. Sreejith, and H. R. Hatwar (2011), Impact of MJO on the intraseasonal variation of summer monsoon rainfall over India, *Clim. Dyn.*, *36*, 41–55.
Périgaud, C., and P. Delecluse (1992), Annual sea level variations in the southern tropical Indian Ocean from Geosat and shallow-water simulations, *J. Geophys. Res.*, *97*(C12), 20,169–20,178, doi:10.1029/92JC01961.
Qiu, Y., W. Cai, L. Li, and X. Guo (2012), Argo profiles variability of barrier layer in the tropical Indian Ocean and its relationship with the Indian Ocean dipole, *Geophys. Res. Lett.*, *39*, L08605, doi:10.1029/2012GL051441.
Saji, N. H., B. N. Goswami, P. N. Vinayachandran, and T. Yamagata (1999), A dipole mode in the tropical Indian Ocean, *Nature*, *401*, 360–363.
Saji, N. H., S.-P. Xie, and C.-Y. Tam (2006), Satellite observations of intense intraseasonal cooling events in the tropical south Indian Ocean, *Geophys. Res. Lett.*, *33*, L14704, doi:10.1029/2006GL026525.
Sardessai, S., S. Shetye, M. V. Maya, K. R. Mangala, and S. Prasanna Kumar (2010), Nutrient characteristics of the water masses and their seasonal variability in the eastern equatorial Indian Ocean, *Mar. Environ. Res.*, *70*, 272–282, doi:10.1016/j.marenvres.2010.05.009.
Schiller, A., and J. S. Godfrey (2003), Indian Ocean intraseasonal variability in an ocean general circulation model, *J. Clim.*, *16*, 21–39.
Seiki, A., M. Katsumata, T. Horii, T. Hasegawa, K. J. Richards, K. Yoneyama, and R. Shirooka (2013), Abrupt cooling associated with the oceanic Rossby wave and lateral advection during CINDY2011, *J. Geophys. Res. Oceans*, *118*, 5523–5535, doi:10.1002/jgrc.20381.
Sengupta, D., G. N. Bharath Raj, and S. S. C. Shenoi (2006), Surface fresh water from Bay of Bengal runoff and Indonesian Throughflow in the tropical Indian Ocean, *Geophys. Res. Lett.*, *33*, L22609, doi:10.1029/2006GL027573.
Shinoda, T., and H. H. Hendon (1998), Mixed layer modeling of the intraseasonal variability in the tropical western Pacific and Indian oceans, *J. Clim.*, *11*, 2668–2685.
Shinoda, T., H. Hendon, and J. Glick (1998), Intraseasonal variability of surface fluxes and sea surface temperature in the tropical western Pacific and Indian Oceans, *J. Clim.*, *11*, 1685–1702.
Song, Q., A. L. Gordon, and M. Visbeck (2004), Spreading of the Indonesian throughflow in the Indian Ocean, *J. Phys. Oceanogr.*, *34*, 772–792.
Sperber, K. R., and D. Kim (2012), Simplified metrics for the identification of the Madden-Julian oscillation in models, *Atmos. Sci. Lett.*, *13*, 187–193, doi:10.1002/asl.378.
Sprintall, J., and M. Tomczak (1992), Evidence of the barrier layer in the surface layer of the tropics, *J. Geophys. Res.*, *97*(C5), 7305–7316, doi:10.1029/92JC00407.
Stephenson, G. R., Jr., S. T. Gille, and J. Sprintall (2012), Seasonal variability of upper ocean heat content in Drake Passage, *J. Geophys. Res.*, *117*, C04019, doi:10.1029/2011JC007772.

Thadathil, P., P. M. Muraleedharan, R. R. Rao, Y. K. Somayajulu, G. V. Reddy, and C. Revichandran (2007), Observed seasonal variability of barrier layer in the Bay of Bengal, *J. Geophys. Res.*, *112*, C02009, doi:10.1029/2006JC003651.

Thompson, D. B., and P. E. Roundy (2013), The relationship between the Madden-Julian Oscillation and U.S. violent tornado outbreaks in the spring, *Mon. Weather Rev.*, *141*, 2087–2095.

Vialard, J., and P. Delecluse (1998), An OGCM Study for the TOGA decade. Part II: Barrier-layer formation and variability, *J. Phys. Oceanogr.*, *28*(6), 1089–1106.

Vialard, J., et al. (2009), Air-sea interactions in the Seychelles-Chagos Thermocline Ridge region, *Bull. Am. Meteorol. Soc.*, *90*, 45–61.

Vinayachandran, P. N., and N. H. Saji (2008), Mechanisms of South Indian Ocean intraseasonal cooling, *Geophys. Res. Lett.*, *35*, L23607, doi:10.1029/2008GL035733.

Waliser, D. E., R. Murtugudde, and L. Lucas (2003), Indo-Pacific Ocean response to atmospheric intraseasonal variability. 1: Austral summer and the Madden-Julian Oscillation, *J. Geophys. Res.*, *108*(C5), 3160, doi:10.1029/2002JC001620.

Webster, P. J., and R. Lukas (1992), TOGA-COARE: The coupled ocean-atmosphere response experiment, *Bull. Am. Meteorol. Soc.*, *73*, 1377–1416.

Woolnough, S. J., F. Vitart, and M. Balmaseda (2007), The role of the ocean in the Madden-Julian Oscillation: Implications for MJO prediction, *Q. J. R. Meteorol. Soc.*, *133*, 117–128.

Xie, S.-P., H. Annamalai, F. A. Schott, and J. P. McCreary (2002), Structure and mechanism of South Indian Ocean climate variability, *J. Clim.*, *15*, 864–878.

Yabuki, T., T. Suga, K. Hanawa, K. Matsuoka, H. Kiwada, and T. Watanabe (2006), Possible source of the Antarctic Bottom Water in the Prydz Bay Region, *J. Oceanogr.*, *62*, 649–655, doi:10.1007/s10872-006-0083-1.

Yoneyama, K., C. Zhang, and C. N. Long (2013), Tracking pulses of the Madden-Julian Oscillation, *Bull. Am. Meteorol. Soc.*, *94*(12), 1871–1891.

You, Y. (1995), Salinity Variability and Its Role in the Barrier-Layer Formation during TOGA-COARE, *J. Phys. Oceanogr.*, *25*, 2778–2807.

Zhang, C. (2005), Madden-Julian Oscillation, *Rev. Geophys.*, *43*, RG2003, doi:10.1029/2004RG000158.

Zhang, C., and M. J. McPhaden (2000), Intraseasonal surface cooling in the equatorial western Pacific, *J. Clim.*, *13*, 2261–2276.